UNCERTAINTY, VALIDATION OF COMPUTER MODELS AND THE MYTH OF NUMERICAL PREDICTABILITY[1]

François M. Hemez[2] and Scott W. Doebling[3]

Engineering Analysis Group (ESA-EA)
Los Alamos National Laboratory
P.O. Box 1663, Mail Stop P946, Los Alamos, New Mexico 87545, U.S.A.

SUMMARY: This publication addresses the issues of modeling, uncertainty quantification, model validation and numerical predictability. With the increasing role of numerical simulation in science, technology as well as every day decision-making, assessing the predictive accuracy of computer models becomes essential. Conventional approaches such as finite element model updating or Bayesian inference are undeniably useful tools but they do not fully answer the question: ***How accurately does the model represent reality?*** First, the evolution of scientific computing and consequences in terms of modeling and analysis practices are discussed. The intimate relationship between modeling and uncertainty is explored by defining uncertainty as an integrate part of the model, not just parametric variability or the lack of knowledge about the physical system being investigated. Examples from nuclear physics and structural dynamics are provided to illustrate issues related to uncertainty, validation and predictability. Finally, feature extraction or the characterization of the dynamics of interest from time series is discussed.

KEYWORDS: Numerical predictability, uncertainty analysis, model validation, design of experiments, feature extraction, parameter calibration, finite element model updating.

I. INTRODUCTION

Today's computational resources make it more than ever possible to model and analyze complex phenomena characterized by complex geometries and boundary conditions, multi-physics, nonlinear effects and variability. An example of such resource is the U.S. Department of Energy's Accelerated Strategic Computing Initiative (ASCI) that has developed several platforms able to sustain over 3 x 10^{+12} operations per second (or 3 TeraOps) by distributing computations over arrays of more than 6,000 processors. The next generation of ASCI computers is expected to reach 30 TeraOps by the

---

[1] This publication is unclassified. Approved for unlimited, public release on May 14th, 2001. LA-UR-01-2492.
[2] Technical Staff Member, hemez@lanl.gov (E-mail), 505-665-7955 (Phone), 505-665-7836 (Fax).
[3] Technical Staff Member, doebling@lanl.gov (E-mail), 505-667-6950 (Phone), 505-665-2137 (Fax).

year 2004 with the goal of approaching 100 TeraOps a few years later. Examples of problems requiring access to these multi-physics codes and massively parallel architectures include global climate prediction, epidemics modeling, computational molecular dynamics, thermo-nuclear physics and complex engineering simulations. Reference [1] discusses the overall ASCI program and its objectives.

In addition to improving computational resources, as we know them today, groundbreaking discoveries are being made in the area of quantum computing, a field thought to be an elegant but impractical theory only a few years ago. This technology enables scientists to store information (bits of zeros and ones) as positive or negative spins of elementary particles that form the building blocks of molecules. Immediate and obvious advantages are infinitely large memory sizes and rapidity of access to the information bounded only by the speed of light. Moreover, the theory of quantum mechanics states that an elementary particle may feature positive and negative spin values simultaneously. Thus, a single particle may potentially store two bits of information at once. Just like a "conventional" computer combines analog bits to perform an operation, a quantum computer would combine the spin values of its elementary particles to add and multiply numbers or search a database. Since one particle can store two pieces of information, two particles can access 2^2 bits. If a very small number of particles can be stabilized, say, no more than 1,000, then this quantum computer could potentially access 2-to-the-power-10^{+3} bits simultaneously. Assuming that the multiplication of two 256-digit numbers involves 10^{+5} bits of information, this translates into 10^{+48} TeraOps of computing power for a single molecule! Practical difficulties such as verification algorithms and the instability of this information storage technology (typically, a particle may randomly change its spin value as often as every 10^{-15} seconds) are currently being addressed at Los Alamos and other national laboratories and university research centers.

Quantum computing will probably not offer any practical outcome for several decades but it is undeniable that unprecedented computational resources are becoming available. What will be the impact on our modeling capabilities and analysis practices?

Obviously, the hypothesis sustaining the development of ASCI-class computing resources is that predictive accuracy can be achieved if enough "details" and "physics" can be included in the numerical simulation. For example, physicists and mecanicians are increasingly involved in the development and implementation of constitutive models at the microscopic and nano-scale levels based on basic physics (or "first principles") such as statistical quantum mechanics. The intent is to capture the physics of interest at the source rather than relying on global and somewhat arbitrary quantities generally defined in solid mechanics such as modal damping ratios.

In addition to demonstrating that complex phenomena can be coupled together and simulated numerically, scientists are increasingly becoming concerned with the predictive accuracy of their numerical models. This emerging field is often referred to as ***model validation***. Here, the central question is: ***How accurately does the model represent reality?*** It consists of determining the predictive quality of numerical simulations and assessing the degree of confidence with which models can be analyzed outside of their nominal operating conditions. Caution must however be exercised to avoid the common confusion between model ***verification*** and model ***validation***. For example, consider ancient Greek astronomy. The models developed by Pythagoras, Aristotle and Ptolemy between 500 BC and 300 BC dominated Western astronomy for nearly 2,000 years. They exhibited

various levels of complexity but all shared the characteristic that our Sun and other planets of our solar system did gravitate around the Earth. These models were somewhat consistent with each other, they fulfilled their purpose of predicting with remarkable accuracy the cycles of seasons and they even matched physical observation. Yet, they were not accurate representation of reality.

In this work, we conform to the U.S. Department of Energy's definition of verification and validation where, basically, ***verification*** consists of verifying that equations are solved correctly while ***validation*** consists of verifying that the equations implemented provide an acceptable representation of reality. This publication discusses the concepts of modeling, uncertainty, model validation and predictability in the context of large-scale numerical simulations. The discussion is illustrated using an engineering application currently dealt with at Los Alamos National Laboratory. References [2-4] offer additional details regarding the particular analysis techniques and results to which the discussion refers.

II. CONCEPTUAL VIEW OF MODELING AND UNCERTAINTY

In this work, uncertainty is defined as the omitted or unknown part of a mathematical model. This definition is somewhat different from the parametric variability or lack-of-knowledge views generally agreed upon in the scientific community. It is also implied that numerical simulations should always include a representation of the uncertainty associated with a particular model. This is consistent with our approach to model validation that states that there is no such thing as model "validation" because all that statistical testing can assess is the degree to which a model breaks down, not the degree to which a model works.

To illustrate how model order truncation and uncertainty are related to the process of modeling a given phenomenon, we consider the example of two elementary particles interacting with each other. This is a common problem in quantum mechanics further complicated by extreme uncertainty (the well-known Heisenberg principle states that position accuracy is bounded by momentum uncertainty, and vice-versa) and large scaling differences (heavy particles interact with much lighter particles). Credit must be given to Reference [5] for originally discussing this example in the context of uncertainty analysis. Our system is formed of two particles, $\mathbf{X_1}$ and $\mathbf{x_2}$, interacting with each other. The first particle denoted by $\mathbf{X_1}$ is the primary system of interest. Its dynamic is influenced by a secondary particle denoted by $\mathbf{x_2}$. We have no real interest in predicting the dynamic of $\mathbf{x_2}$ but it is included in the equations because of the interaction with the main degree-of-freedom. The equations of motion considered are:

$$\frac{\partial^2 \mathbf{X_1}}{\partial \mathbf{t}^2} + \mathbf{?}_1^2(\mathbf{1} + \mathbf{x_2^2})\mathbf{X_1} = \mathbf{0}, \qquad \mathbf{e}^2 \frac{\partial^2 \mathbf{x_2}}{\partial \mathbf{t}^2} + \mathbf{?}_2^2(\mathbf{1} + \mathbf{X_1^2})\mathbf{x_2} = \mathbf{0} \tag{1}$$

In the numerical application, values of $\mathbf{?}_1$ and $\mathbf{?}_2$ are kept constant and equal to one. The initial conditions of the primary particle $\mathbf{X_1}$ are set to one for displacement and zero for velocity. Initial conditions in both displacement and velocity for the secondary particle $\mathbf{x_2}$ are uncertain and vary uniformly among 13 discrete values $\{10^{-1}; 3x10^{-1}; 7x10^{-1}; 1; 3; 7; 10^{+1}; 3x10^{+1}; 7x10^{+1}; 10^{+2}; 3x10^{+2}; 7x10^{+2}; 10^{+3}\}$. Another important characteristic of the system of equations (1) is that the secondary particle is very light compared to the other one. The mass of the secondary particle is $\mathbf{e^2 = 10^{-6}}$ times

smaller than the mass of the primary particle. This introduces ill-conditioning and convergence difficulties when, for example, Runge-Kutta finite differences are implemented to solve the system of partial differential equations (1). Figure 1 illustrates the output when equations (1) are integrated numerically in time. The top figure shows the position $\mathbf{X_1}$ and the bottom figure shows the position $\mathbf{x_2}$. Note the amplitude difference in position between the two degrees-of-freedom. Displacements of the secondary particle are approximately three orders of magnitude smaller. As the second mass becomes smaller, the response $\mathbf{x_2}$ becomes rapidly varying and suitable for statistical treatment.

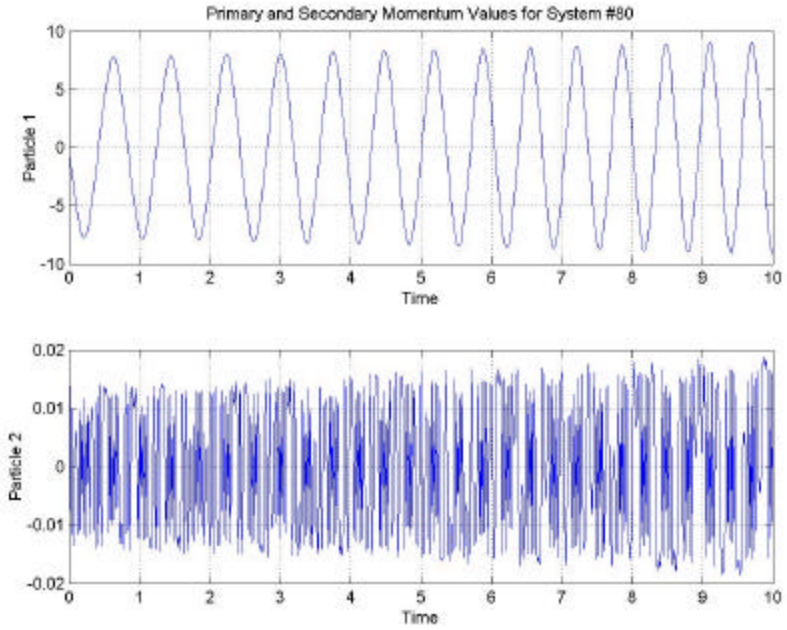

Fig. 1: Responses of the Two Degrees-of-freedom System.
(Top: Displacement of the primary particle $\boldsymbol{X_1}$. Bottom: Displacement of the secondary particle $\boldsymbol{x_2}$. Initial conditions are set to {1; 7} for displacements and {0; 0.3} for velocities.)

We start by solving the fully coupled equations (1) for all possible combinations of initial conditions for the secondary particle. The position and momentum of particle $\mathbf{x_2}$ can assume 13 discrete values each, which leads to a full factorial analysis of $13^2 = 169$ systems. Figure 2 illustrates the position of particle $\mathbf{X_1}$ versus time obtained for the 10^{th}, 60^{th}, 100^{th} and 150^{th} systems. It can be observed that the system of equations (1) spans a wide range of dynamics. Responses range from linear, single degree-of-freedom oscillators (top left) to damped, linear systems (top right) and systems featuring time varying, higher-frequency harmonics (bottom left). The forth system (bottom right) exhibits chaotic behavior and a component that eventually grows unstable. Being able to characterize the dynamics of responses is an important step of model validation. Feature extraction is further addressed in section V. The information generated by solving the equations (1) for all possible combinations of initial conditions is summarized in Figure 3. It shows the most probable state of each particle in the position-momentum plane. The most probable states of the primary particle $\mathbf{X_1}$ are shown on the top half while those of the secondary particle $\mathbf{x_2}$ are shown on the bottom half. Hence, Figure 3 illustrates the output variability obtained by propagating uncertain initial conditions through the forward calculation.

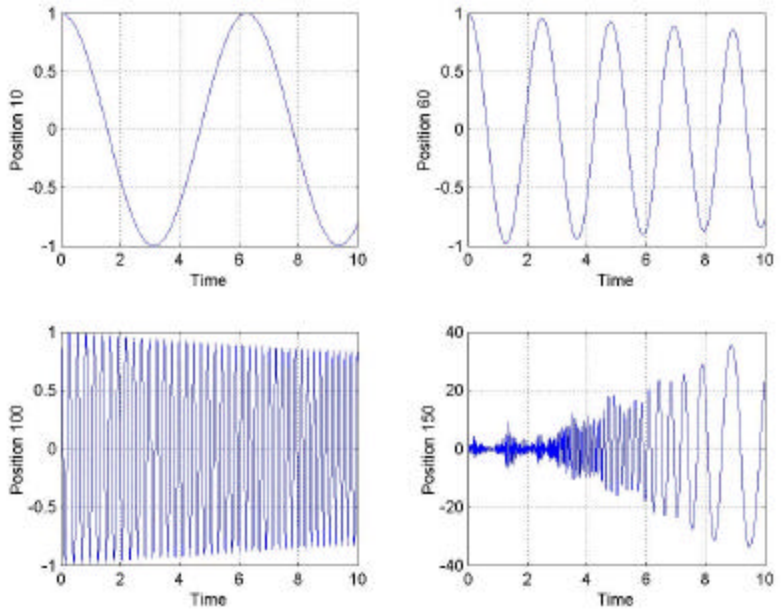

Fig. 2: Four Typical Responses of the Two Degrees-of-freedom System.
(Initial conditions for $\boldsymbol{X_1}$ *and its momentum are kept constant and equal to (1; 0). Initial conditions for* $\boldsymbol{x_2}$ *and its momentum are as follows. Top Left: IC =* $(10^{-1}; 10^{-3})$*. Top Right: IC =* $(1; 3x10^{-5})$*. Bottom Left: IC =* $(10; 7x10^{-5})$*. Bottom Right: IC =* $(10^{+2}; 10^{-5})$*.)*

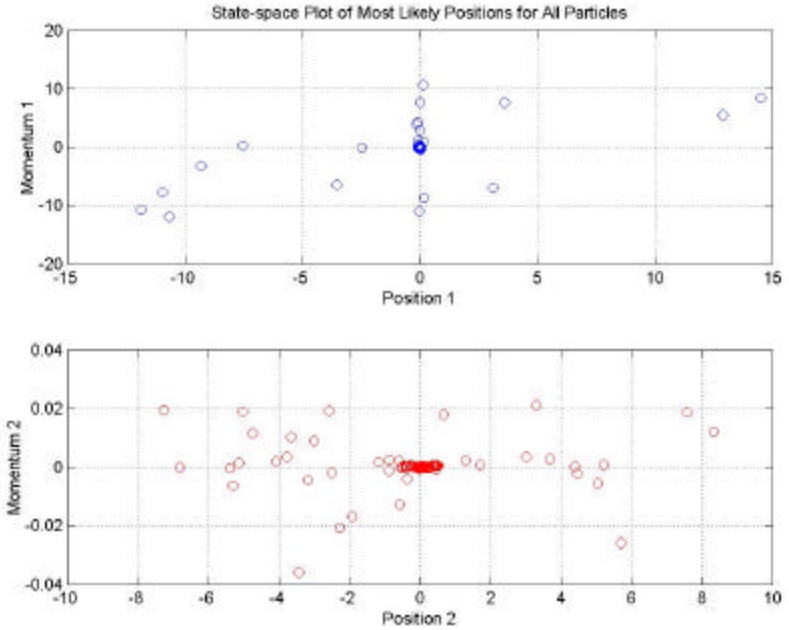

Fig. 3: Most Probable Position-Momentum States of Particles $\boldsymbol{X_1}$ *and* $\boldsymbol{x_2}$*.*
(Top: Mean state values of particle $\boldsymbol{X_1}$*. Bottom: Mean state values of particle* $\boldsymbol{x_2}$*. Note that numerical values are plotted on different horizontal and vertical scales. Also noticeable are the different correlation structures of the joint probability distributions of particles 1 and 2.)*

The dynamics of particle $\mathbf{X_1}$ is now represented as a single degree-of-freedom linear oscillator. The coupling with particle $\mathbf{x_2}$ is completely ignored and replaced by a random process. This illustrates situations where the correct model order is unknown or the model of interaction between particles $\mathbf{X_1}$ and $\mathbf{x_2}$ is not available. Obviously, integrating the time response of particle $\mathbf{X_1}$ based on a linear oscillator representation would result into large prediction errors. However, unavailable modeling information can advantageously be replaced by probabilistic information. Figure 4 pictures the most probable position-momentum states of the 169 systems for the full factorial analysis. Solutions obtained with uniform distributions are shown on the top half and solutions obtained with normal distributions are shown on the bottom half. Both results can be compared to the "true" solution shown in Figure 3 (top half). It can be observed from a comparison of Figures 3 and 4 that the correlation structure between position and momentum is lost. This is expected because the physics-based coupling is replaced with an arbitrary random process. Nevertheless, the approximated solutions are consistent with the true solutions. Another advantage is that the linear oscillator equations can be solved in a fraction of the time required to integrate the coupled equations (1) because they are well posed.

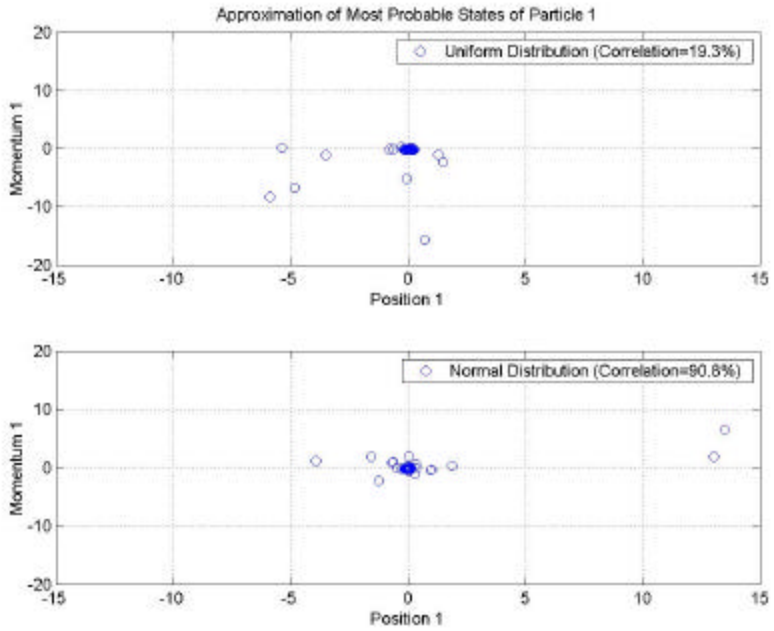

Fig. 4: Most Probable States of Particle $\boldsymbol{X_1}$ With Coupling Approximated.
(The figure shows the mean position and momentum values of particle $\boldsymbol{X_1}$ obtained for each one of the 169 systems when the coupling term with particle $\boldsymbol{x_2}$ is replaced by a random process. Top: Uniform distributions. Bottom: Normal distributions.)

Uncertainty originates from several practices commonly adopted during modeling such as selecting an inadequate model form, truncating the model order, approximating equations and introducing parametric variability. Uncertainty cannot be dissociated from modeling. Attempts to explain a complex physical experiment by mathematical models define uncertainty. Computer simulations should therefore not be attempted without including a representation of the uncertainty associated with modeling assumptions. This implicitly defines model validation as an exercise where the consistency between model output and reality is assessed away from the model's nominal operating ranges. The two-particle

example illustrates that potentially missing information can be replaced by adequate statistical treatment. Since a random process can always be parameterized, hyper-parameters such as the mean, variance, covariance structure and higher-order statistics can be calibrated to improve the predictability of the computer simulation. An illustration of model calibration via Bayesian inference is provided in section III.

We have mentioned that missing information can be replaced by probabilistic information. Other frameworks are available for quantifying and propagating uncertainty that may offer attractive alternatives to the theory of probability especially in the event of extreme uncertainty. Among them, we cite the Dempster-Shafer theory of possibility and belief [6], the theory of fuzzy sets [7], information gap theory and convex models of uncertainty [8]. In the remainder, uncertainty is represented by probability density functions. This is a reasonable assumption when dealing with physics or engineering applications where reasonable amounts of test data are available and the systems investigated are governed by well-established theories.

III. PREDICTABILITY IN COMPUTATIONAL SCIENCES

Currently, all computational sciences are, to various degrees, struggling with the notion of numerical predictability, uncertainty quantification and model validation. The reason is because scientists are increasingly relying on numerical models to make predictions and replace physical measurements. As the computer models grow in size and complexity, so does the need to assess their validity especially when full-scale testing is not available. To illustrate these trends, an example from nuclear physics is provided. It involves the inference of a time-varying parameter from uncertain measurements.

When fissionable materials are assembled, the system can become critical, that is, neutron fluxes can grow exponentially. The measure of this criticality is a parameter known as the Rossi alpha. It is defined as the rate at which the neutron flux grows:

$$\mathbf{a(t)} = \frac{\mathbf{1}}{\mathbf{y(t)}} \frac{\partial \mathbf{y(t)}}{\partial \mathbf{t}} = \frac{\partial \mathbf{ln(y(t))}}{\partial \mathbf{t}} \tag{2}$$

In equation (2), the symbols **a(t)** and **y(t)** denote the Rossi alpha parameter and the neutron flux, respectively. To develop a numerical model of criticality, the value of **a(t)** must be inferred from the measurement of Rossi traces $\mathbf{y(\cos(2\pi f_R t))}$. Because the neutron flux increases rapidly during a criticality experiment, the time variable is replaced by a pseudo-time $\mathbf{\cos(2\pi f_R t)}$. Figure 5 illustrates a typical amplitude growth of a neutron flux.

The inverse problem thus consists of obtaining the value of **a(t)** that best reproduces the test data $\{\mathbf{x_k}; \mathbf{y_k}\}$. One formulation among others is Bayesian inference. It has shown great success for this particular application and details about the procedure can be obtained from References [9-10]. First, a parametric model is chosen for representing the unknown function **a(t)**. This model translates the prior knowledge about the Rossi alpha and depends on unknown parameters that are collectively denoted by the symbol **?**. Next, the sources of uncertainty must be assessed and propagated. The main uncertainty for this application resides in the placement of data points from measurement readings. Each point

shown in Figure 5 is typically associated with uncertainty in the x-direction and y-direction. For simplicity, we denote by $\mathbf{s}_x$ and $\mathbf{s}_y$ the standard deviations corresponding to the placement of data $\mathbf{x_k}$ and $\mathbf{y_k}$, respectively. This assumes that uncertainty in the placement of points in the (x; y) plane is uncorrelated, which is an assumption that test data generally do not support. If the correlation $\mathbf{?_{xy}}$ can be ignored, a natural metric that expresses the "distance" between test data and numerical simulation is represented by the minus-log likelihood of the observed data given the current model:

$$\mathbf{logP(x_k; y_k \mid a)} = -\sum_{\mathbf{k=1\cdots N_{data}}} \left(\frac{\mathbf{x_k^{Test} - x_k(a)}}{\sqrt{2}\mathbf{s}_x} \right)^2 + \left(\frac{\mathbf{y_k^{Test} - y_k(a)}}{\sqrt{2}\mathbf{s}_y} \right)^2 \tag{3}$$

Other potential sources of uncertainty, not accounted for in equation (3) for clarity, might include uncertainty in the nature of the parametric model used to represent the Rossi alpha parameter **a(t)** and uncertainty in the hyper-parameters **?**. Smoothness parameters are typically included in the set **?** to control the prior knowledge about the problem. Prior knowledge plays the same role as "regularization" in the resolution of ill-posed inverse problems. Equation (3) also assumes that statistical distributions are normally distributed which does not have to be the case.

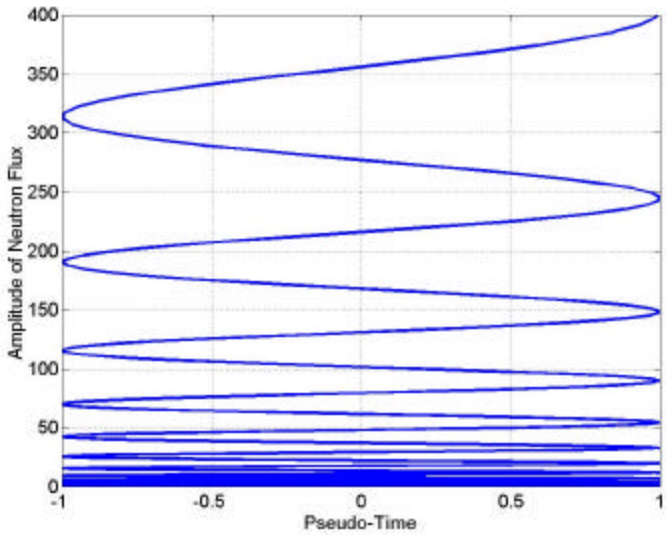

Fig. 5: Amplitude Growth of a Neutron Flux During Criticality.
(The amplitude of a neutron flux is illustrated on a log-scale as a function of $\boldsymbol{\cos(2\pi f_R t)}$ *where* $\boldsymbol{f_R}$ *denotes the Rossi frequency. The shape of the curve is characteristic of physical measurements, however, the values are numerically simulated for the purpose of this illustration.)*

Inference of the model **a(t)** and, potentially, inference of the unknown hyper-parameters **?**, is achieved according to the Bayes law that states that the posterior distribution of the model given the available data or $\mathbf{P(a \mid x_k; y_k)}$ is equal to the likelihood function $\mathbf{P(x_k; y_k \mid a)}$ multiplied by the prior distribution **P(a)**:

$$\mathbf{P(a \mid x_k; y_k) = P(x_k; y_k \mid a)\, P(a)} \tag{4}$$

The objective naturally becomes to maximize the posterior distribution, which translates that the model sought is the one that is most consistent with test observation. Similarly, the posterior distribution of hyper-parameters given the data or $\mathbf{P(? \mid x_k; y_k)}$ can be maximized to infer the value of hyper-parameters **?** that are most consistent with test data. At this point, an optimization solver can be implemented to maximize the posterior distributions $\mathbf{P(a \mid x_k; y_k)}$ or $\mathbf{P(? \mid x_k; y_k)}$. One particularly attractive choice is the Markov Chain Monte Carlo (MCMC) algorithm. The MCMC method generates a random sequence of parameters **a(t)** that samples the posterior distribution $\mathbf{P(a \mid x_k; y_k)}$. The main advantage of the MCMC optimization is that sampling can be carried out independently of the distribution being sampled. In particular the assumption of normal probability distribution, which is encountered in many formulations for the only purpose of allowing tractable analytical derivations, is irrelevant. For more details, the reader is referred to Reference [11] where a tutorial of MCMC methods is provided. Figure 6 illustrates three realizations of **a(t)** obtained through MCMC sampling of the Bayesian posterior distribution (4).

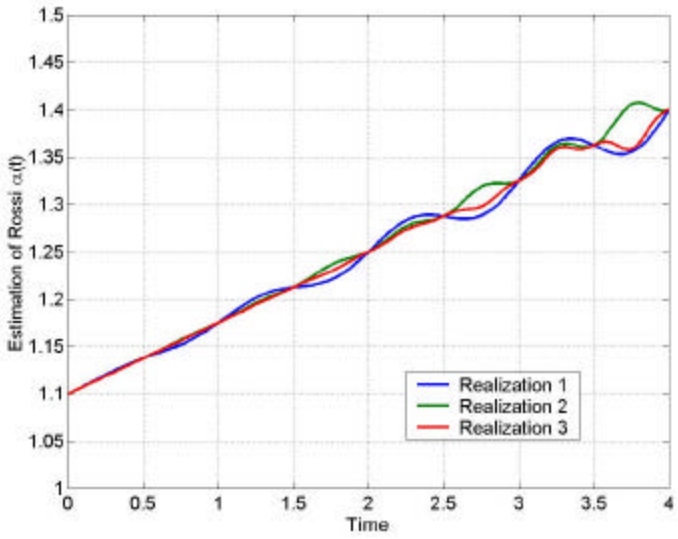

*Fig. 6: MCMC Inference of Rossi Alpha **a(t)** From the Bayesian Posterior.*
*(The figure illustrates that several optimal solutions can be obtained that are statistically consistent with physical measurements. If enough independent samples can be drawn from the posterior distribution, basic statistics about the inferred parameter **a(t)** can also be estimated.)*

The purpose of this example is to illustrate inverse problem solving. In the presence of uncertainty, several optimal solutions can be obtained that remain consistent with the physical observation. Exploring the posterior distribution therefore becomes critical. If enough independent samples can be drawn from the posterior probability distribution, basic statistics about the inferred parameters—mean, variance, covariance structure, etc.—can be estimated. Hence, the uncertainty observed through physical experimentation can be related to parametric variability of the model, which is important information for design and decision-making.

Bayesian inference represents one of many possible formulations among which we cite maximum likelihood, Mahanalobis hypothesis testing, Kullback-Leibner entropy and Chernov entropy. The statistical techniques developed for hypothesis testing or group classification can generally be applied to

formulate inference problems. Methods such as finite element model updating, parameter identification and parameter calibration (also referred to as parameter "tuning") all fall under this general description. However, we stress that a ***calibrated*** model by no means constitutes a ***validated*** model, as commonly accepted in the finite element updating community. Validation is fundamentally a statement about ***predictability*** whereas calibrated models are, at best, only able to match physical measurements at one or several design points.

IV. ASCI ENGINEERING APPLICATIONS

Quantifying shock transmission through complex, jointed structures has traditionally been possible only with experimental methods. These experiments are expensive and time-consuming and thus only a few cases can be studied. With the advent of large scale computing capabilities, estimation of the shock transmission with numerical models is becoming a tractable problem. The ASCI computing environment is being used at Los Alamos to study, among other things, the transmission of these shocks through complex, jointed structures. This on-going experiment is summarized to illustrate the validation of engineering applications in structural dynamics.

4.1 The Forward Mount Impulse Test

The test article used for the validation experiment consists of several components fabricated from a variety of materials. A titanium component designated the "mount" is shown in Figure 7 (top left). All other components are connected to the titanium mount. The upper payload mass simulator, which is fabricated from 6061-T6 aluminum, is bolted to the three feet on the upper end of the mount. The lower payload mass simulator, which is fabricated from carbon steel, is held inside the mount using a tapered tape joint. The tapered tape is fabricated from SS-304 stainless steel and is inserted through the thin, horizontal slot near the base of the mount. Separate pieces of the tapered tape are driven in, wedging the mass simulator against an inner retaining surface. All these components are pictured in Figure 7 (bottom left).

The lower shell, fabricated from 7075-T4 aluminum, and then anodized, is placed over the titanium mount and its rim sits on a ledge just below the threaded portion of the mount. Next, a titanium retaining nut threads onto the titanium mount bearing against the upper surface of the lower shell rim. A specified torque value is applied. Finally, the upper shell, also fabricated from aluminum, is threaded onto the mount. As this second specified torque is applied, the load between the retaining nut and lower shell is somewhat reduced.

Figure 7 (right) also shows that the test article is suspended using wire rope. This creates a pendulum with a length of about one meter. Pendulum motion is monitored using high-speed photography and fiber optic-based displacement sensing. An explosive source is developed to apply an impulsive load to a portion of the outside surface of the test article. The source is fabricated from strips of thin explosive sheet material. The explosive strips are simultaneously initiated using an explosive lens. The pressure at the surface of the test article is moderated with a buffer material made from solid neoprene. Prior to

testing, the explosive load underwent a careful characterization to make sure that the correct impulse was measured.

Fig. 7: Forward Mount and Other Components of the Assembly.
(Top Left: Titanium forward mount. Bottom Left: Other components of the assembly. From left to right, lower shell; titanium mount and bolted mass simulator; retaining nut and upper cylindrical shell. Right: Instrumented system, explosive grid and testing fixture.)

The test article is instrumented with 33 strain gages and 6 accelerometers. The strain gages are attached to the inside surface of the titanium mount and have an active length of 0.8 mm to obtain localized effects. The six accelerometers are Endevco model 7270A-200k and are located on either end of both payload mass simulators. Four are oriented laterally in the direction of the delivered impulse and two are oriented along the axis of the structure. Measured strains range up to 1.0% and have a frequency response of 100 KHertz. Peak accelerations after low-pass filtering at 50 KHertz range up to 10,000 g's. The comparison of strain and acceleration responses in Figure 8 (left) indicates that the shock wave rapidly propagates through the main joint. The ringing of the mass simulators is attenuated after 5-to-6 milliseconds. The sixth acceleration response is used to define the input excitation of a shock response spectral (SRS) analysis. The SRS in Figure 8 (right) shows the peak acceleration response that would be witnessed by a single degree-of-freedom system whose fundamental frequency is set by the horizontal axis. Clearly, most of the resonant dynamics occur between 10 and 30 KHertz, which would make analysis techniques based on modal superposition impractical. The SRS estimates the acceleration levels that would be witnessed, for example, by an electronic component.

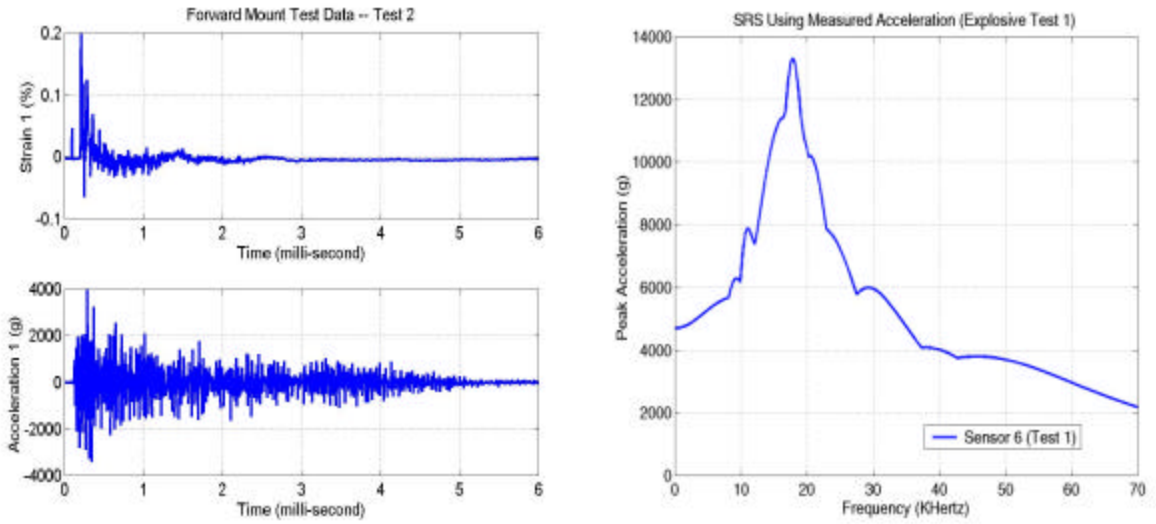

Fig. 8: Typical Impulse Response of the Forward Mount Test Article.
(Top Left: Strain 1 located behind the explosive grid. Bottom Left: Acceleration 1 located on the lower mass simulator. Right: SRS of the 6th acceleration response with 2% modal damping.)

Figure 9 compares the strain responses collected at location 1 (inside the mount, behind the explosive grid) during two replicate tests. Only the first 400 microseconds of response after detonation are shown. It can be observed that the peak strain and "low-frequency" content are very similar. The discrepancy between the two curves is attributed to the variability of the experiment. The main source of variability is a tolerance and assembly-positioning threshold that is controlled during these two experiments. The comparison illustrates that, in addition to predicting the dynamics of interest, the numerical model should also reproduce the variability inferred from physical observations when replicate data sets are available.

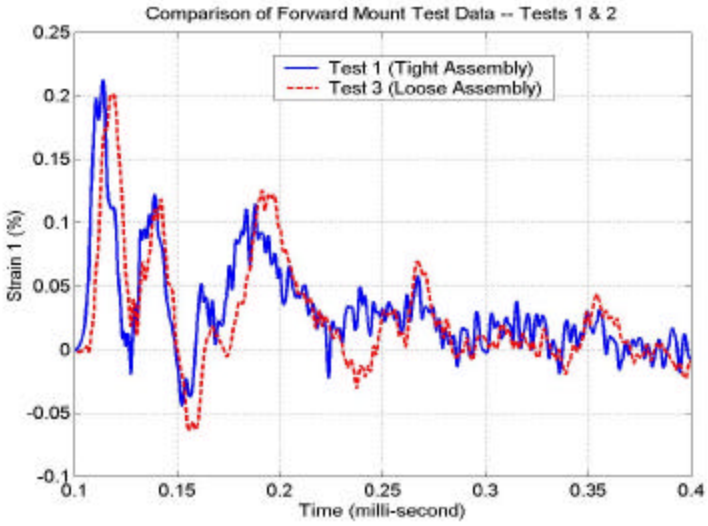

Fig. 9: Comparison of Strain Responses Collected During Two Similar Tests.
(Responses of strain sensor 1 located behind the explosive grid. Solid, blue line: Response when the assembly is closely controlled. Dashed, red line: Response with a "loose" assembly.)

4.2 Finite Element Modeling and Analysis

The explicit finite element model of the test article is developed using the ParaDyn finite element code [12]. In general, explicit formulations are preferred for such problems because of their nonlinear nature and the fact that numerous contact conditions must be handled. The model has approximately 1.4 million 8-node hexahedral elements, 56,000 4-node shell elements, 480 contact surfaces and 1.8 million node points. It results into 6 million degrees of freedom that include structural displacements and Lagrange multipliers defined at the contact interfaces. The large number of contact pairs is required because each individual surface, usually circumferential in nature, has to be broken into several individual surfaces to accommodate efficient partitioning for the parallel code. Automatic contact capabilities that are currently under development in ParaDyn will obviate the need to break the contact into so many surfaces. The computational mesh is illustrated in Figure 10. The finite element model is currently run on 504 processors on the Los Alamos Blue Mountain ASCI computer. Using this number of processors results in 1.3 CPU hours for each millisecond of simulation.

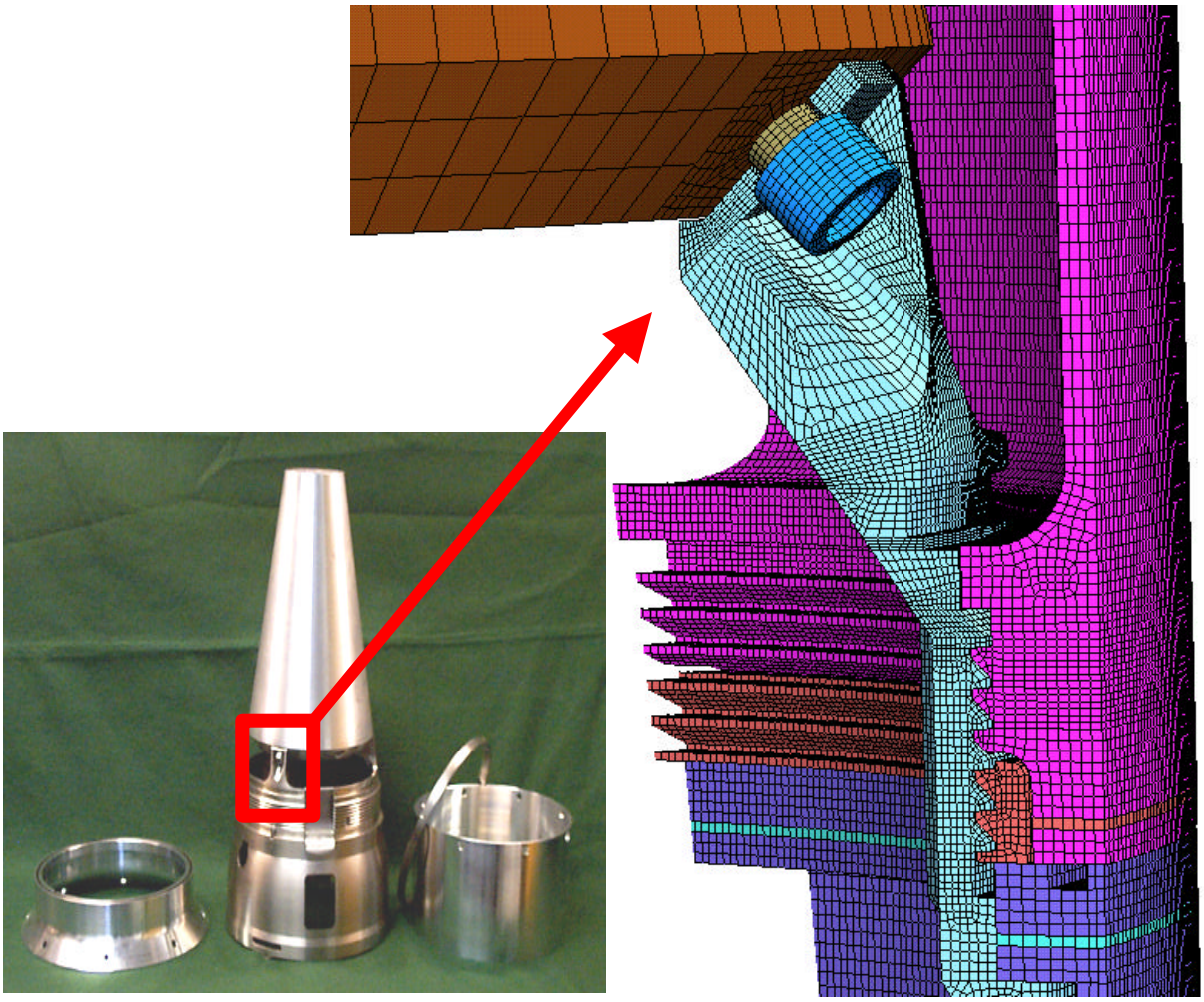

Fig. 10: Computational Mesh of the Threaded Joint and Bolts.
(Viewed from the inside of the titanium mount, one of the upper mass simulator's bolts and a section of the retaining nut are visible between the assembly of upper and lower shells.)

Preloading due to assembly of the threaded joints and the tape joint is accomplished in the model by implementing an orthotropic thermal coefficient of expansion in specific layers of elements. At the start of each analysis, the temperature is increased using a half-cosine time history over 0.2 milliseconds. The structure is then allowed to freely respond with no additional input for 0.1 milliseconds before applying the explosive impulse. The impulse is applied over the appropriate region of the test article as a pressure time history.

4.3 Uncertainty Analysis

Because the contact involves interfaces among stainless steel, carbon steel, anodized 7075-T4 aluminum, 6061-T6 aluminum, and titanium, precise selection of static and kinetic coefficients of friction is not possible. Some of the variables that contribute to the coefficients of friction include surface finish, surface hardness and the presence of lubricants. Since these are not known, these coefficients of friction are estimated by bounds and allowed to vary between specified limits. Lacking a precise definition of the coefficients of friction also leads to unknown levels of preloads. Therefore, the preloads are also allowed to vary between specified limits among the different runs. Based on engineering judgment, a total of twelve parameters are defined as having a relatively high uncertainty associated with their value. These parameters consist of three component preloads, four static and four kinetic coefficients of friction and the magnitude of the explosive impulse.

In this section, we illustrate one of the steps that would be involved in a typical validation experiment. A parameter effect analysis is performed to determine which of the twelve input parameters are most responsible for explaining the total variability of the output. Other steps, not discussed here, would include parametric calibration, characterization of the model output's probability information and assessment of the model's predictive quality. All these analyses share the need to generate ***response surface models*** (RSM) to replace the expensive, large-scale simulations [13]. Four of the twelve input parameters of interest can take two possible values and the remaining eight parameters can take three possible values. The total number of runs to build a full factorial analysis would therefore be equal to $2^4 \times 3^8 = 104{,}976$, a number that would require nearly 8 years of computational time using 6,000 processors of a 3 TeraOps ASCI platform! To limit the required simulation time, a subset of 48 runs is completed from parameter samples selected using the Taguchi orthogonal array technique [14]. After these 48 runs have been completed and the appropriate features have been extracted, a statistical RSM of the form

$$\mathbf{y} = \mathbf{a}_o + \sum_{i=1\cdots12} \mathbf{a}_i \mathbf{p}_i + \sum_{i=1\cdots12} \sum_{j=1\cdots12, j\geq i} \mathbf{ß}_{ij} \mathbf{p}_i \mathbf{p}_j \qquad (5)$$

is fit to the computer data for each feature of interest. The difference with a conventional response surface is essentially that statistical testing and ***analysis of variance*** (ANOVA) techniques are used to retain only the most significant interaction parameters $\{\mathbf{a}_i; \mathbf{ß}_{ij}\}$. Linear and second-order coefficients $\mathbf{a}_i$ and $\mathbf{ß}_{ij}$ are defined as statistics whose probability information is available for further statistical treatment such as re-sampling and hypothesis testing. When no other option is available but an extremely sparse

sampling of the input space, special care must be brought to selecting a design matrix that avoids ***aliasing***. Aliasing in statistical modeling refers to contamination of main (linear) effects by secondary (higher-order) effects and is caused by a too sparse sampling matrix. Obviously, any sampling matrix must provide the ability to distinguish the variance associated with the linear effect of a variable from the other variables. But it can happen that linear effects (such as $\mathbf{a_i}$) are confounded or aliased with second order or higher effects (such as $\mathbf{ß_{ij}}$). With a Taguchi orthogonal array, columns of the design matrix are not correlated with other columns and, in addition, are free of interaction with second-order effects. This makes for efficient linear screening.

Because the transmission of shock across the mount to the payload components is the primary event of interest, errors between the predicted and measured statistical moments of the time history, shock response spectrum and power spectral density (PSD) at each accelerometer location are used as features. Time histories are restricted to the first four milliseconds following detonation and the SRS and PSD analyses are performed from 0-to-50 KHertz with a uniform 2% critical damping for the SRS. The first and second statistical moments (mean and standard deviation) are investigated. Hence, a total of 36 output features are defined (6 accelerometers x 3 criteria x 2 moments). For each one of them, a linear statistical RSM is constructed. Statistical tests are implemented to assess the global contribution of each input parameter to the total variability observed from the computer simulations. A popular example is the R-square (R^2) statistics that estimates Pierson's correlation ratio. It is defined as the ratio between the variance that can be attributed to a given effect and the total variance of the data [15]:

$$\mathbf{R^2 = 1 - \frac{\sum_{l=1\cdots N_{level}} \sum_{j=1\cdots N_{data}^{(l)}} \left(y_j^{(l)} - \bar{y}^{(l)}\right)^2}{\sum_{j=1\cdots N_{data}} \left(y_j - \bar{y}\right)^2}} \tag{6}$$

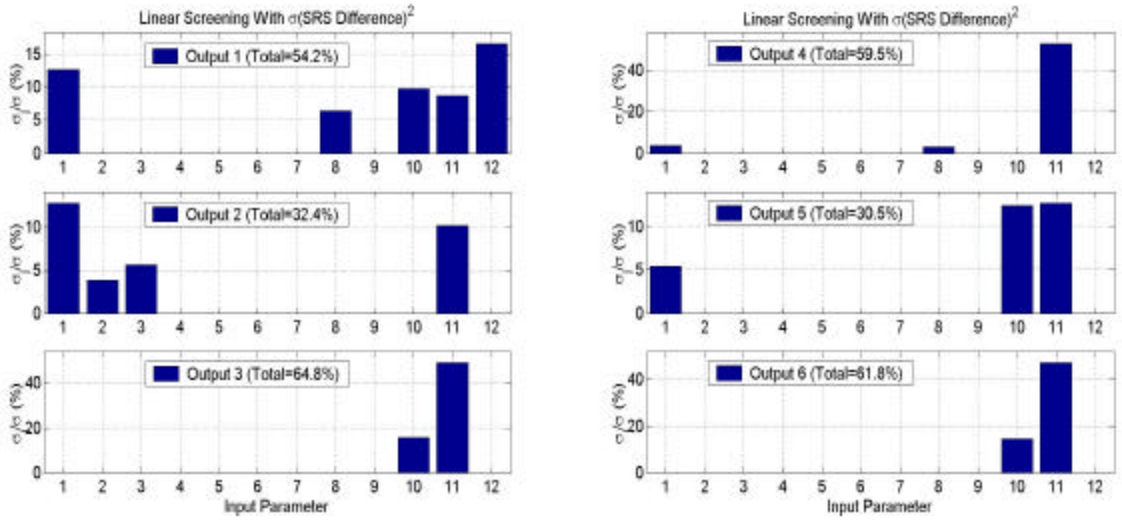

Fig. 11: Parameter Contributions Calculated From the Analysis of Variance.
(Left: ANOVA of accelerations 1-3. Right: ANOVA of accelerations 4-6. The feature analyzed is the variance s^2 of the difference between predicted and measured SRS. Percentages show the contribution of each input parameter to the total variance of the output feature.)

A trend is observed for features from all sensors indicating significant effects due to the following five parameters: one preload ($\mathbf{p_1}$), three kinetic coefficients of friction ($\mathbf{p_8}$, $\mathbf{p_{10}}$, $\mathbf{p_{11}}$) and the impulse magnitude ($\mathbf{p_{12}}$). The R^2 values obtained by analyzing the standard deviation of SRS errors are pictured in Figure 11. The six acceleration locations exhibit global sensitivity to at least one of the five parameters $\mathbf{p_1}$, $\mathbf{p_8}$, $\mathbf{p_{10}}$, $\mathbf{p_{11}}$ and $\mathbf{p_{12}}$. For location 2, the other two preloads $\mathbf{p_2}$ and $\mathbf{p_3}$ are significant but this linear RSM only explains 32.4% of the output feature's total variance. Linear models that do not explain at least 50% of the total variance are considered suspect and higher-order parameter interactions should be included. This analysis demonstrates that the parameter space can be reduced from a dimension equal to twelve to a dimension equal to five, therefore, allowing realistic generation of a higher-order RSM's.

V. FEATURE EXTRACTION

In this section, the notion of ***feature extraction*** is discussed. Features are defined as small-dimensional quantities that extract information from physical observation or computer output. Obviously, their definition is application-dependent and they should satisfy two other criteria. First, a feature must provide insight regarding the physics investigated. Second, it must be sensitive to changes in the input parameters, whether "sensitivity" is defined locally or as a global parameter effect (R^2 and other statistics, ANOVA, etc.).

In linear structural dynamics, conventional features are resonant frequencies, modal damping ratios and mode shape vectors. Nevertheless, their application is restricted to stationary and periodic signals generated from the response of linear systems. Because non-linearity is increasingly investigated, attempts are made to generalize the notion of modal superposition to nonlinear dynamics, for example, using the wavelet transform and the proper orthogonal decomposition. Success is documented in Reference [16] (wavelet transform) and Reference [17] (Karhunen-Loève transform), among others. However, these analysis techniques remain based on the assumption of linearity and their application to non-stationary data sets or nonlinear systems is necessarily limited. One of the reasons why slow progress is made in areas such as condition diagnostics and health monitoring of complex engineering systems is because the features employed do not characterize the dynamics of interest with enough accuracy. Another reason often mentioned is that conventional features are not sensitive enough to local condition changes such as crack propagation or boundary condition change. Our opinion is that tools commonly used in other scientific communities (e.g. physics, statistical sciences and pattern recognition) are not exploited to their full potential.

The applicability of pattern recognition techniques is first illustrated using an Earthquake example that has recently been publicized and widely distributed over the Internet [18]. On February 28, 2001, a magnitude 6.8 Earthquake located thirty miles below the surface and a few miles away from Olympia, Washington, moved the ground for 30-to-40 seconds. The recorded Earthquake waveform is shown in Figure 12 (top). A sand-tracing pendulum located in the vicinity produced the patterns depicted in Figure 12 (bottom right). The smooth curves seen to the outside of the Earthquake "rose" are what is normally observed when someone sets the pendulum in motion to make a tracing. The pattern produced when the pendulum was started prior to the Earthquake is still visible. It was then overwritten by another

pattern resulting from ground motion. Clearly, the difference between these two patterns indicates different dynamics more so than a direct comparison between, for example, time series or shock response spectra.

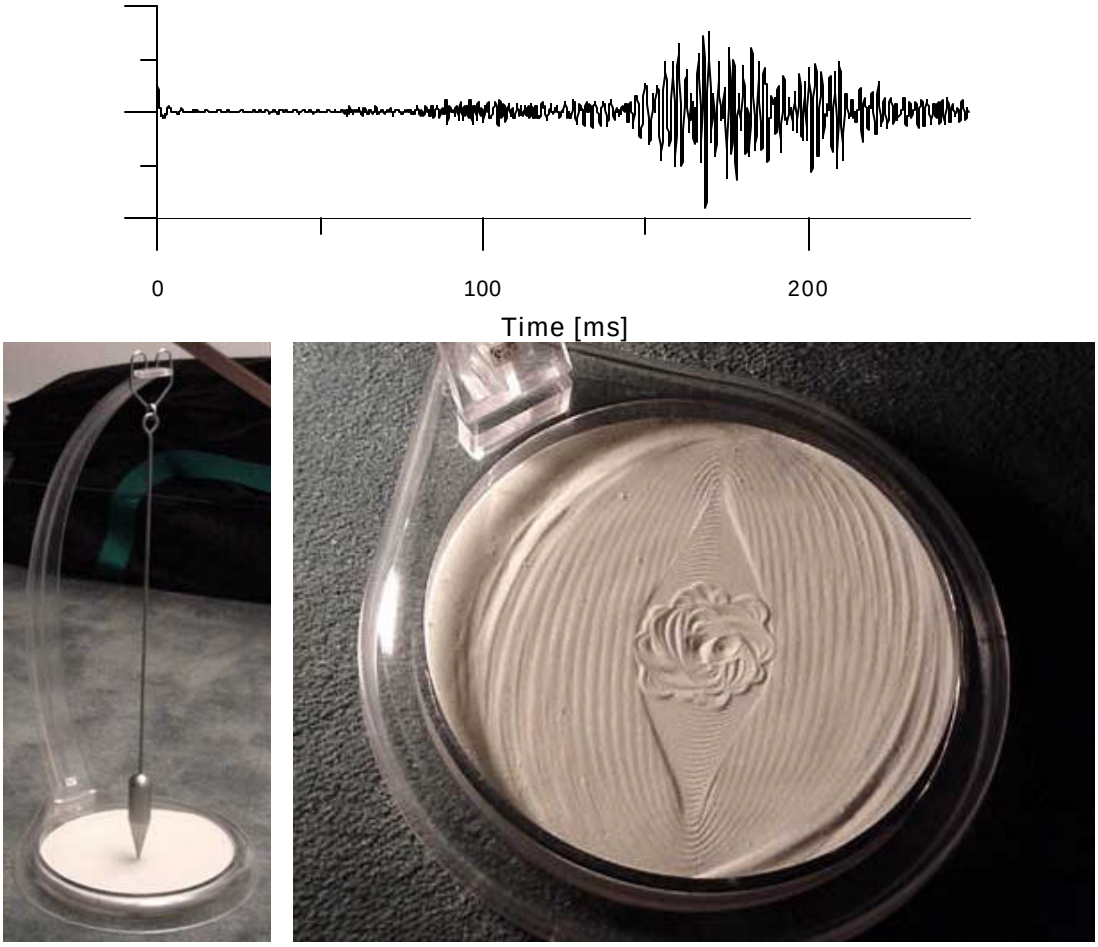

Fig. 12: Records of the February 28, 2001 Earthquake at Olympia, Washington. (Top: Time-domain signal. Bottom Left: Sand-tracing pendulum. Bottom Right: Patterns produced by the pendulum. The pendulum performs a transform of the original signal analogous to phase-amplitude decoupling. A steady-state periodic signal produces the circle-like pattern seen on the outside. The transient Earthquake signal produces the twisted pattern at the center.)

The mathematical transformation implemented by the pendulum is very similar to the state-space representation of a symmetric dot pattern transform. Its efficiency for characterizing complex dynamics is further illustrated with the two-particle interaction model. Consider the four signals **y(t)** shown in Figure 2. They can be transformed into $\mathbf{z(t) = a(t)e^{jf(t)}}$ where $\mathbf{j^2 = -1}$ and the amplitude **a(t)** and phase **f (t)** components are defined as:

$$\mathbf{a(t)} = \frac{\left(\mathbf{y(t)} - \mathbf{y_{min}}\right)}{\left(\mathbf{y_{max}} - \mathbf{y_{min}}\right)}, \quad \mathbf{f\ (t)} = \mathbf{?} + \mathbf{?}\frac{\left(\mathbf{y(t+t)} - \mathbf{y_{min}}\right)}{\left(\mathbf{y_{max}} - \mathbf{y_{min}}\right)} \tag{7}$$

The symmetric dot pattern method transforms the correlation between values **y(t)** and **y(t+t)** distant of a time shift **t** into polar coordinates. This transformation is used in the field of speech recognition to express visually, in an easy-to-understand figure, the changes in amplitude and frequency content of sound signals. An application to fault diagnosis is presented in Reference [19] where the transformation is implemented to diagnose changes in sound signals between health and faulty bearings. In our example, the angle shift **?** is set to 60 degrees, the amplification factor **?** is set to 10.0 and the time shift **t** is equal to 1/500th of the time record's length. These parameters are determined somewhat arbitrarily. When transformed, the previous four time series produce the patterns shown in Figure 13. An immediate advantage is normalization. While the horizontal and vertical scales are all different in Figure 2, the four subplots of Figure 13 are contained between –1 and +1, which makes for a convenient comparison. Significant differences can be observed between the patterns produced by the linear signals (top) and the nonlinear signals (bottom). The chaotic response is also different from the other three as indicated by the peculiar distribution of points in the complex plane.

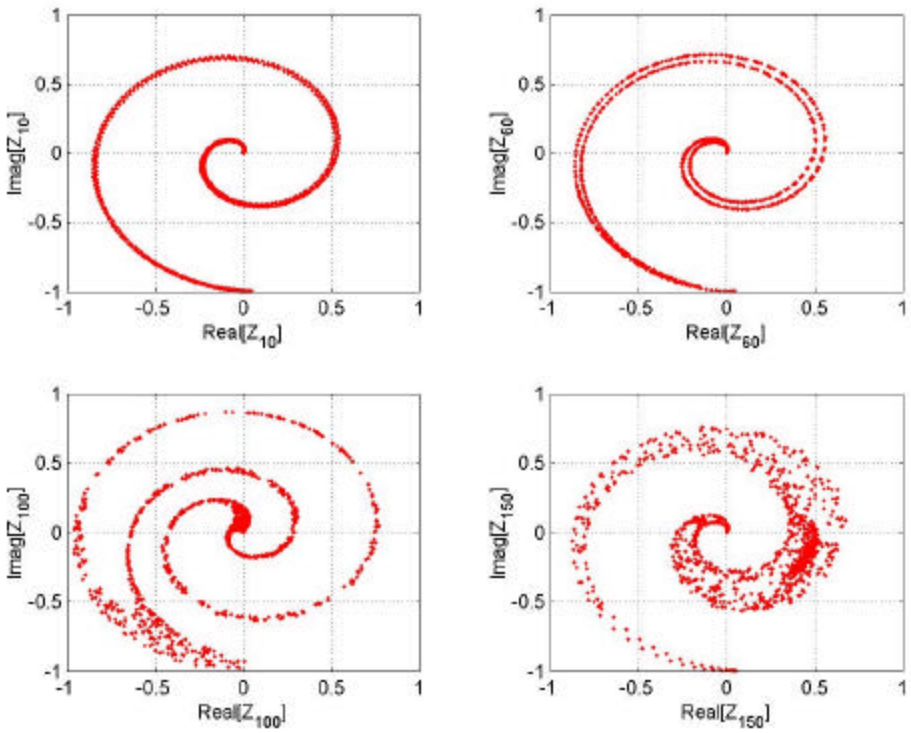

Fig. 13: Symmetric Dot Patterns From the Two-particle Systems.
(Upper Left: System 10; single mode, low-frequency response. Upper Right: System 60; single mode, lightly damped response. Lower Left: System 100; high-frequency response with time-varying frequency. Lower Right: System 150; chaotic and unstable response.)

Comparisons such as those illustrated in Figures 2 and 13 are visually appealing but graphics do not provide a quantitative assessment of the difference between data sets. Quantitative measures are needed for inference and parametric calibration. This is because inverse problems are generally formulated as optimization problems. One solution is to train surrogate models to recognize the difference between images and to relate the changes observed to characteristics of the original models

or experiments. This is typically how pattern and image recognition techniques proceed [20]. The alternative is to further condense the information into low-dimensional features. This is essentially what modal frequencies achieve for linear, periodic systems. However, real systems are likely to exhibit complex dynamics that combine nonlinear, non-periodic, non-stationary and chaotic behaviors. Although many signal processing techniques cannot accommodate this complexity, tools such as fractal analysis are available that can.

The fractal of a signal is defined as one of its topological dimension. It represents the number of degrees-of-freedom of the corresponding data set in a multi-dimensional space. Obviously, the fractal of a smooth curve is one, that of a surface is two, etc. Rigorous mathematical definitions are available for more complicated data sets [21]. Fractal models are appropriate for analyzing signals that exhibit some form of self-similarity (for example, statistical), strong irregularity and structure on a global scale as well as arbitrarily fine scales. An application is detailed in Reference [21] where an input-output model of cavitation diagnosis is constructed between the fractal dimension of acoustic pressure measurement and the degree of cavitation in a pump. One estimate of the fractal dimension is provided by the Higuchi method that models the average evolution of the signal's increment coefficients $?_{k,p}$. Increments for samples distant of **k** intervals in time are computed as:

$$?_{k,p} = \frac{N-1}{k^2 ?(N;k;p)} \sum_{i=1\cdots ?(N;k;p)} \left| y(p+ik) - y(p+(i-1)k) \right| \tag{8}$$

where **?(N;k;p)** is defined as the lower integer part of **(N-p/k)**. The index denoted by **p** in equation (8) allows multiple estimates on a single time series and **k** denotes the time shift considered. The increment coefficients $?_{k,p}$ are averaged over the values of indices **p** and the Higuchi model assumes a linear relationship (on a log-log scale) between $\langle ?_k \rangle$, the averaged increment coefficient at index **k**, and the time shift index **k**:

$$\langle ?_k \rangle = a k^{-D} \tag{9}$$

A simple least-squares fit can be performed to estimate the fractal dimension **D**. Note that the fractal dimension must, by definition, be an integer even if its numerical estimation is not.

Figure 14 (left) illustrates the data points $\langle ?_k \rangle$ as a function of the time shift **k**. The other half of Figure 14 (right) shows the fractal dimension **D** estimated for each system. The curves shown on the left of Figure 14 correspond to the four responses of Figures 2 and 13. The mean $\langle ?_k \rangle$ is plotted in solid line and the 2-s confidence intervals are shown in dashed lines. Very little variability can be observed, meaning that the fractal character of the curve is consistent throughout the analysis. The model assumed in equation (9) states that straight lines of slopes equal to **–D** should be observed. This is especially the case for the linear responses 10 and 60.

On the right of Figure 14, three main categories of dynamics can be observed. When the initial momentum ranges from 10^{-1} to 1, little energy is provided by the secondary particle x_2 and the two-particle model behaves as a single degree-of-freedom. The corresponding fractal dimension is logically found close to one. The second category of dynamic systems corresponds to cases where the energy

inputted by the light particle $\mathbf{x_2}$ is significant enough to influence the heavy particle $\mathbf{X_1}$. Then, the system is truly a two-particle system. Figure 14 shows that the fractal dimension is close to two when the initial momentum ranges from $3x10^{+1}$ to $3x10^{+2}$. The last category of dynamic behavior is chaotic with a fractal dimension that oscillates between one and two. This is because the dynamics of these systems transition very rapidly from single degree-of-freedom linear (**D = 1**) to multiple degrees-of-freedom nonlinear and chaotic (**D = 2**). It corresponds to cases where the initial momentum of particle $\mathbf{x_2}$ is equal to $7x10^{+2}$ or greater. Except for the case of chaotic behavior, the estimated fractal is insensitive to the initial position and only the level of energy inputted by particle $\mathbf{x_2}$ matters.

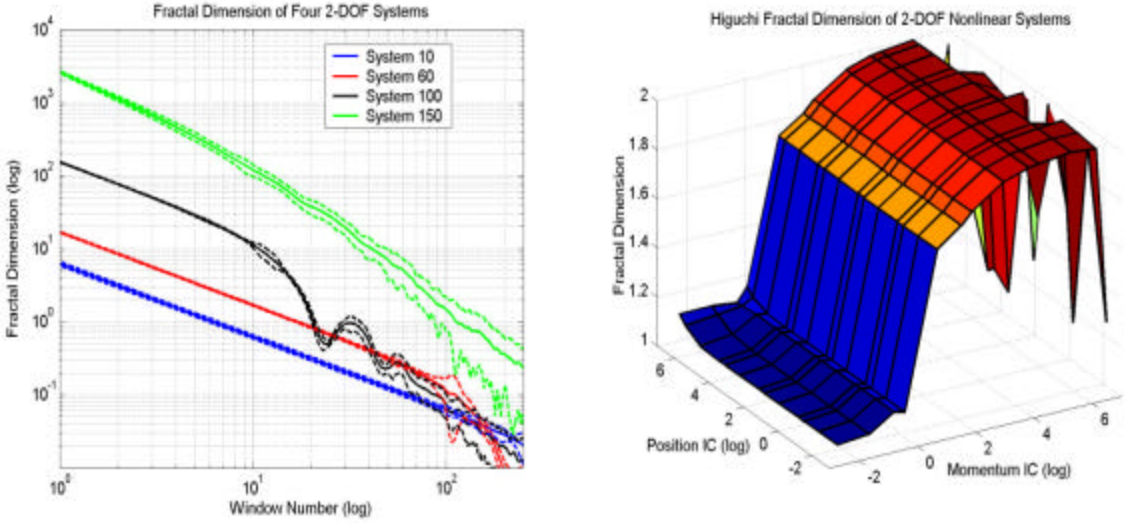

Fig. 14: Increments and Fractal Dimensions of the Two-particle Systems.
*(Left: Signal increments <?$_k$> versus time shift **k**. Right: Fractal dimensions **D** for each system. Shown on the left and from bottom to top are the average increment curves for the 10th, 60th, 100th and 150th systems. Shown on the right are the fractal dimensions for all 169 systems.)*

This example illustrates that powerful features can be implemented that can effectively characterize a wide variety of dynamic behaviors. Of course, we cannot stress enough the importance of selecting features that are relevant to the application investigated and useful to the analyst. Time-frequency analysis techniques encountered in structural dynamics include the power spectral density, power cepstrum, cyclo-stationarity analysis, Willer-ville transform, wavelet transform, spectrogram and Karhunen-Loève decomposition. Many time-frequency analysis techniques, however, are based on assumptions that real-world signals may not always satisfy. General-purpose features can alternatively be extracted from probability density functions, shock response spectra, temporal and statistical moments (mean, variance, energy, kurtosis, etc.) and fractal analysis. In addition, features can be extracted from parametric models best fitted to data sets. The model fitting techniques that have been applied to engineering mechanics problems with success include linear regression (such as AR, ARX), nonlinear regression (such as ARMA), neural networks, statistical models and kriging models.

VI. CONCLUSION: CAN NUMERICAL PREDICTABILITY BE ASSESSED?

This publication discusses the concepts of modeling, uncertainty quantification, model validation and numerical predictability. Not only does uncertainty refer to parametric variability and lack of knowledge, but it can also be seen as an integral component of the numerical model. In light of this conception of uncertainty, model validation is defined as an attempt to identify regions of the design space where the model "breaks down" or uncertainty is too important. Predictability refers to the ability to quantify the accuracy of the model in regions of the design space where physical observations are not available. Model validation must rely on carefully planed experiments that provide an assessment of reality for the largest possible array of configurations and operational conditions. Parametric calibration is a pre-requisite that permits to reduce some of the discrepancy between physical observation and model output but under no circumstance should a calibrated model be considered validated. The issue of feature extraction, or how to characterize the dynamics of time series, is also discussed and the efficiency of a few techniques is illustrated with a simple model of elementary particle interaction.

The ultimate goal of uncertainty analysis and model validation experiments is to guarantee that numerical models accurately represent reality, especially when testing is not an option. In addition, confidence in the prediction must be assessed. Assessing predictability based on validation experiments is an area of open research to a great extent. Reference [22] develops a Bayesian melding framework for statistical inference of simulation models that integrates diagnostic checking, model validation, hypothesis testing and model selection methods. The approach proposed builds on conventional Bayesian inference, goes beyond parametric calibration but stops short of addressing the predictability issue. Another interesting attempt is made in Reference [23]. The authors present a calibration technique that integrates the notion of predictive confidence regions by quantifying and propagating residual errors between calibrated models and experimental data sets. By systematically quantifying all sources of uncertainty, their procedure can assess the prediction's confidence regions and monitor model inadequacy errors.

To the question ***"Can numerical predictability be assessed?"*** our opinion is therefore a cautious yes given that adequate validation experiments are performed. However, this is a difficult problem, far from being resolved. The aforementioned techniques are currently being investigated at Los Alamos for assessing the predictive accuracy of computer codes for hydrodynamic and structural mechanics applications.

ACKNOWLEDGEMENTS

The author would like to acknowledge the contribution of Thomas A. Butler, Scott W. Doebling and John F. Schultze (ESA-EA, Engineering Analysis). They are responsible for most of the ASCI engineering application work discussed in this publication. The author is grateful to Mark C. Anderson (DX-5, Experimentation and Diagnostic Design), Kenneth M. Hanson (CCS-2, Scientific Computing) and Michael D. McKay (D-1, Statistical Sciences) for sharing their thoughts and expertise on model validation. We also acknowledge the support of the weapons program and the ASCI project at Los Alamos for supplying the resources needed to support this work. Los Alamos National Laboratory is operated by the University of California for the U.S. Department of Energy under contract W-7405-ENG-36.

REFERENCES

1. Garcia, J., "The Need For Computational Model Validation," *SEM Experimental Techniques*, Vol. 25, No. 2, March-April 2001, pp. 31-33.

2. Hemez, F.M., Wilson, A.C., Doebling, S.W., "Design of Computer Experiments For Improving an Impact Test Simulation," *19th SEM International Modal Analysis Conference*, Kissimmee, Florida, February 5-8, 2001, pp. 977-985.

3. Butler, T.A., Hemez, F.M., Schultze, J.F., Sohn, H., Doebling, S.W., "Model Validation For a Complex Jointed Structure," *19th SEM International Modal Analysis Conference*, Kissimmee, Florida, February 5-8, 2001, pp. 1318-1324.

4. Doebling, S.W., Butler, T.A., Schultze, J.F., Hemez, F.M., Moore, L.M., McKay, M.D., "Validation of Transient Structural Dynamics Simulations: An Example," *3rd International Conference on Sensitivity Analysis of Model Output*, Madrid, Spain, June 18-20, 2001, to appear.

5. Kast, A., "Dynamic Uncertainty," *19th SEM International Modal Analysis Conference*, Kissimmee, Florida, February 5-8, 2001. Special invited presentation at the SD-2000 session on uncertainty quantification and model validation developed by Hemez, F.M., Doebling S.W., pp. 1153-1158.

6. Yager, R.R., Kacprzyk, J., Fedrizzi, M., **Advances in the Dempster-Shafer Theory of Evidence**, John Wiley & Sons, New York, 1996.

7. Dumitrescu, D., Jain, L.C., Lazzerini, B., **Fuzzy Sets and Their Application to Clustering and Training**, International Series on Computational Intelligence, CRC Press, New York, 2000.

8. Ben-Haim, Y., Cogan, S., Sanseigne, L., "Usability of Mathematical Models in Mechanical Decision Processes," Mechanical Systems and Signal Processing, Vol. 12, No. 1, January 1998, pp. 121-134.

9. Hanson, K.M., Booker, J., "Inference From Rossi Traces," *Oral Presentation at the Los Alamos Uncertainty Quantification Working Group*, Los Alamos National Laboratory, Los Alamos, New Mexico, September 2000. http://www.lanl.gov/home/kmh/.

10. Hanson, K.M., Cunningham, G.S., "Posterior Sampling With Improved Efficiency," *Proceedings of the SPIE Conference*, Vol. 3338, 1998, pp. 371-382.

11. Gilks, W.R**., Markov Chain Monte Carlo in Practice**, Chapman and Hall, New York, 1996.

12. Hoover, C.G., De Groot, A.J., Sherwood, R.J., "ParaDyn: A Parallel Nonlinear, Explicit, Three-Dimensional Finite-Element Code for Solid and Structural Mechanics—User Manual," *LLNL UCRL-MA Report*, Lawrence Livermore National Laboratory, Livermore, California, 2000.

13. Myers, R.H., Montgomery, D.C., **Response Surface Methodology: Process and Product Optimization Using Designed Experiments**, Wiley Inter-science, New York, 1995.

14. Hedayat, A.S., Sloane, N.J.A., Stufken, J., **Orthogonal Arrays: Theory and Applications**, Springer-Verlag, New York, 1999.

15. McKay, M.D., Beckman, R.J., Conover, W.J., "A Comparison of Three Methods For Selecting Values of Input Variables in the Analysis of Output From a Computer Code," *Technometrics*, Vol. 21, No. 2, 1979, pp. 239-245.

16. Dalpiaz, G., Rivola, A., "Condition Monitoring and Diagnostics in Automatic Machines: Comparison of Vibration Analysis Techniques," *Mechanical Systems and Signal Processing*, Vol. 11, No. 1, January-February 1997, pp. 53-73.

17. Lenaerts, V., Kerschen, G., Golinval, J.C., "Parameter Identification of Nonlinear Mechanical Systems Using Proper Orthogonal Decomposition," *18th SEM International Modal Analysis Conference*, San Antonio, Texas, February 7-10, 2000, pp. 133-139.

18. MacLeod, N., "The Earthquake Rose," *Web Report*, March 2001. http://www.gaelwolf.com/pendulum.html.

19. Shibata, K., Takahashi, A., Shirai, T., "Fault Diagnosis of Rotating Machinery Through Visualization of Sound Waves," *Mechanical Systems and Signal Processing*, Vol. 14, No. 2, March-April 2000, pp. 229-241.

20. Bishop, C.M., **Neural Networks for Pattern Recognitio**n, Oxford University Press, New York, 1998.

21. Simard, P., Le Tavernier, E., "Fractal Approach For Signal Processing and Application to the Diagnosis of Cavitation," *Mechanical Systems and Signal Processing*, Vol. 13, No. 3, May-June 2000, pp. 459-469.

22. Poole, D., Raftery, A.E., "Inference for Deterministic Simulation Models: The Bayesian Melding Approach," *Technical Report No. 346*, Department of Statistics, University of Washington, Seattle, Washington, December 1998. http://www.stat.washington.edu/raftery/.

23. Kennedy, M.C., O'Hagan, A., "Bayesian Calibration of Computer Models," *Journal of the Royal Statistical Society (Series B*), 2001, to be published. http://www.shef.ac.uk/~st1ao/.